Automated Detection of Martian Dune Fields

Lourenço Bandeira, Jorge S. Marques, José Saraiva, and Pedro Pina

***Abstract*—An approach for the automated detection of dune fields on remotely sensed images of the surface of Mars is presented in this letter. It is based on the extraction of local information from images (i.e., gradient features), which, in turn, is tested with boosting and support vector machine classifiers. A detection rate of about 95% is obtained for fivefold cross validation on a set of 78 panchromatic images captured by the Mars Orbiter Camera of the Mars Global Surveyor probe on different locations of the planet.**

***Index Terms*—Boosting, dunes, histogram of oriented gradient (HOG) features, Mars, support vector machine (SVM).**

I. Introduction

WIND is the most important erosive agent on present-day Mars, and the availability of large amounts of loose sand and dust provides conditions for the existence of dune fields all over the planet. Studying these, the most frequent aeolian features on the Martian landscape, contributes to the understanding of interactions between the atmosphere and the surface of the plane. Their study can also provide clues about the evolution of the climate on Mars [1], [2].

Large dune fields on Mars were first observed in 1971 on Mariner 9 images [3], [4]. However, only recent imagery has led to the identification of countless small dune fields [5] and to the confirmation that the shapes visible show many similarities with those occurring on Earth [6].

The recently created Mars-Dune.org Consortium (http://www.mars-dunes.org) has the stated intention to produce a catalog containing all dune fields identifiable on the surface of Mars [6]. This endeavor demands a huge effort and cooperation among planetary scientists to enlarge the database, deepen the knowledge on these features, and improve our understanding of the fundamental processes underlying their formation. This manually constructed database contains, at the moment of writing, information between latitudes 90° N and 65° S [7], [8]. A rough estimation of the area covered by dune fields on Mars is about 900 000 km^2, and although most large fields have been already mapped, the countless smaller ones have not, which leads to a figure of about 90% of the Martian dune fields still in need of analysis [9].

The huge quantity and dynamic characteristics of these aeolian features call for an automated method that is able to delineate them on remotely sensed images whatever their scale. Some recent techniques have been developed to automatically detect structures on optical images of planetary surfaces. Attention has been mainly devoted to impact crater detection, and some very good results have been achieved [10]–[12], whereas research into dune identification has been less prominent. Still, methods for temporal change detection [13]–[15] or measurement of dune heights [16], [17] and morphologies [18] have been developed, although normally restricted to geographically confined regions both on Earth and Mars.

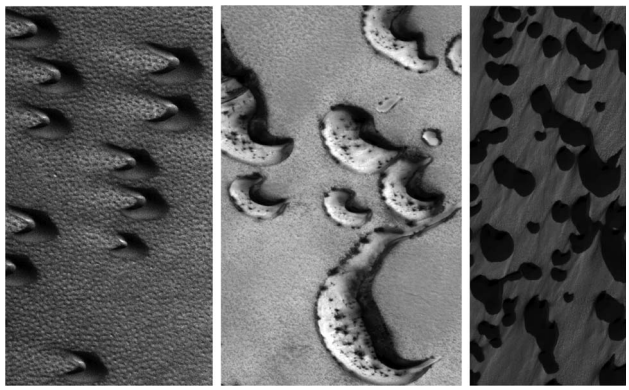

Fig. 1. Variety of barchan and barchanoid dunes on Mars on Mars Global Surveyor/MOC images (from left to right): E01-01867, E18-00494, and S01-00925. Each image covers an area of 1500×3000 m^2 [image credits: Malin Space Science System (MSS)/National Aeronautics and Space Administration (NASA)/Jet Propulsion Laboratory (JPL)].

Thus, our objective is to use state-of-the-art machine learning methodologies for the detection of aeolian dunes on remotely sensed images of Mars. This letter is partly inspired on previous strategies and algorithmic sequences used for automated crater detection [11] while being a continuation of preliminary tests where we verified the relevance of automated methods for the detection of sand dunes [19]. In this letter, we consider two types of features that excel in the extraction of the directional and periodic characteristics of the dunes (i.e., gradient and histogram of oriented gradient (HOG) features), which are then used on boosting and support vector machine (SVM) classifiers to decide if a given region of the image contains dunes.

II. Problem Formulation

The dunes so far identified on the Martian surface have been generally classified according to a geological classification scheme put forward by McKee [20] for terrestrial examples, considering the different shapes that exist and relating them to specific environments of deposition and factors acting upon it. Although most of them fit into the main types, there are some undefined morphologies not known to commonly occur on Earth [6].

In Fig. 1, we present some examples of the two predominant Martian dune types, namely, barchan and barchanoid. The first type consists of crescent-shaped structures (example on the left

Manuscript received June 16, 2010; revised September 6, 2010 and November 2, 2010; accepted December 2, 2010. Date of publication January 19, 2011; date of current version June 24, 2011. This work was supported in part by the Foundation for Science and Technology of Portugal under Project PTDC/CTE-SPA/110909/2009 and Scholarships SFRH/BD/40395/2007 (LB) and SFRH/BD/37735/2007 (JS).

L. Bandeira, J. Saraiva, and P. Pina are with the Centre for Natural Resources and the Environment, Instituto Superior Técnico, 1049-001 Lisboa, Portugal (e-mail: lpcbandeira@ist.utl.pt; jose.saraiva@ist.utl.pt; ppina@ist.utl.pt).

J. S. Marques is with the Institute for Systems and Robotics, Instituto Superior Técnico, 1049-001 Lisboa, Portugal.

Color versions of one or more of the figures in this paper are available online at http://ieeexplore.ieee.org.

Digital Object Identifier 10.1109/LGRS.2010.2098390

image), whereas the second refers to more or less parallel rows of coalesced crescents (example on the right image); the center image represents an intermediate stage between individual barchans and the coalesced barchanoids. From these simple examples, it already becomes clear that there are a multitude of factors affecting the visual aspect of dune fields—for instance, tone of constituent particles, angle of illumination, size, shape, density, association to seasonal advance/withdrawal of ice cover, just to name some—that must be tackled by any automated approach designed to detect their presence in an image. Thus, the nature and varied characteristics of occurrence of sand dunes in images of the Martian surface demand a learning strategy that is able to adapt itself to distinct situations.

The procedure adopted for the identification of the dunes is based on the analysis of local information of the image along a regular grid. For that purpose, an image is divided into cells from which given features will be extracted. To increase the invariance to specific factors such as illumination and shadowing, an aggregation of the local features is performed within larger regions, i.e., blocks constituted by 3×3 cells, which are the detection windows. The block window is moved along the whole grid, with a cell-sized step (thus, for instance, adjacent blocks in a row will only differ by a cell column).

III. Methods

Important advances were achieved in the last decade in the field of computer vision, both in the type of features used to characterize objects and in the recognition methods, which are employed to learn and classify the objects present in the images.

From those recent contributions, we selected gradient-based features, which we consider to be among the most appropriate to detect the patterns exhibited by sand dunes.

For block classification, we used two of the most advanced and powerful classifiers that have already proven their ability in dealing with a variety of classification problems, namely, in remotely sensed imagery of planetary surfaces, i.e., boosting and SVM.

A. Feature Extraction

We considered features based on the image gradient $g(x) \in \mathbb{R}^2$ computed at each image point x. The gradient vector is characterized by its amplitude $|g(x)|$ and phase $\phi(x)$. These features are grouped into four sets.

1) *HP(9):* This set corresponds to the HOG features proposed for face detection by Dalal and Triggs [21] and is intended to capture the typical edge structure of the local shape of a dune, with a controlled degree of invariance to local geometric and radiometric factors. To obtain them, it is necessary to compute a weighted histogram of the phase for each cell. All the points in each cell contribute to the phase histogram with a vote, and each vote is proportional to the gradient magnitude. Therefore, the histogram value associated to the kth cell C^k is

$$h_i^k = \sum_{x \in C^k} |g(x)| \cdot b_i\left(\phi(x)\right) \tag{1}$$

where

$$b_i(\phi) = \begin{cases} 1, & \text{if } \phi \in i\text{th bin} \\ 0, & \text{if otherwise.} \end{cases}$$

An angular interval of 20° for the computation of the directional histograms is defined; thus, a total of 81 features per block (9 histogram bins/cell $\times$ 9 cells) are extracted. The phase histograms are not normalized since the features should depend on the amount of texture present in the original cell. If we normalize the histogram (1), a cell without texture could have the same features as a cell with strong texture (gradient magnitude).

2) *HPM(9)*: This set is a modified version of the HOG features by separately using the phase histogram, i.e.,

$$h_i^k = \sum_{x \in C^k} b_i\left(\phi(x)\right) \tag{2}$$

and the magnitude histogram, i.e.,

$$\tilde{h}_i^k = \sum_{x \in C^k} \tilde{b}_i\left(|g(x)|\right) \tag{3}$$

where

$$\tilde{b}_i(|g|) = \begin{cases} 1, & \text{if } |g| \in i\text{th bin} \\ 0, & \text{if otherwise.} \end{cases}$$

For the phase, using the same angular interval of 20°, we have 81 features (9 histogram bins/cell $\times$ 9 cells), and for the magnitude, considering 11 bins (resulting from a four-unit interval between a minimum of 0 and a maximum of 40), we have 99 features (11 histogram bins/cell $\times$ 9 cells). Thus, for this set, a total of 180 features per block are obtained.

3) *HP*: This set refers to the histograms of the gradient phase for each image block b as follows:

$$h_i = \sum_{x \in B} b_i\left(\phi(x)\right) \tag{4}$$

in the same 9 bins (with an angular interval of 20°). Thus, 9 features (9 histogram bins/block $\times$ 1 block) are used in this situation. In this case, the phase votes are not weighted by the gradient magnitude.

4) *HPM:* This set consists of separately using the histograms of a phase, as previously defined for the HP set, and of the magnitude of the gradient on each block separately. The histogram amplitude is given by

$$\tilde{h}_i = \sum_{x \in B} \tilde{b}_i\left(|g(x)|\right). \tag{5}$$

Thus, we have 9 features for the phase (1 histogram $\times$ 9 bins of 20° of angular interval) and 11 features for the magnitude (the same bins of the HP features), giving a total of 20 features extracted for this set.

The images are low-pass filtered using a Gaussian impulse response of size 51×51 pixels with $\sigma = 10$ pixels. The size of each cell is 40×40 pixels and is the same for all images. In order to have the features varying between 0 and 1, a normalization step was performed globally for each image and each individual feature.

B. Classification

Boosting algorithms have proven their worth, achieving remarkable results by combining a large number of weak

classifiers using a weighted majority vote [22]. They are also able to perform feature selection, i.e., to select a subset of informative features for a given problem. This can be done by assuming that each weak classifier depends on a single feature [23]. The application of boosting algorithms in object recognition led to excellent results in very diverse problems as, for instance, face [23] or impact crater [11] detections.

SVMs are kernel methods that use an implicit transformation to a higher dimensional space in order to achieve good separability by means of a linear classifier in the new space [24]. The hyperplane used for separation in the higher dimensional space is chosen in such a way that the so-called margin (the distance to the closest samples in each class) is maximized. The samples determining the margin are called the support vectors. Different transformation kernels can be used, such as Gaussian, polynomial, linear, and circular, yielding different classifiers. To test this classifier, we have used the freely distributed package SVMLight [25]. Several kernels were exploited, but among those with higher performances, we chose the linear kernel since it is the most simple.

IV. Experimental Results

To test our approach, we selected a set of 78 remotely sensed images of the surface of Mars captured by the Mars Orbiter Camera (MOC) (at a narrow-angle mode) of the Mars Global Surveyor probe. Those images are from different locations on the planet, cover a total area of about 5032 km^2, and are representative of the diversity of barchan and barchanoid dunes on Mars. They are single-band images with 256 gray levels and have a spatial resolution between 1.61 and 6.80 m/pixel.

For each image, we constructed ground truth information by manually delineating the dunes therein contained (an example is shown in Fig. 2(a), indicating the "dune" and "not-dune" regions). The assignment of a binary label to a cell partially occupied by a dune is somewhat ambiguous. We used two thresholds to remove the ambiguity when tiling the ground truth into cells. Only the cells containing more than 30% of the dune area were considered as "dune," whereas only the cells with less than 10% of the dune area were considered as "not-dune." The cells with dune areas comprised in the interval 10%–30% were not considered [see Fig. 2(b)].

All automated classifiers were tested by a fivefold cross-validation method, i.e., the total number of images was divided into five subsets (folds) so that each one of those contains approximately the same number of cells corresponding to dunes (for details, see Table I). Four of them were used for training, and the remaining one was used for testing with independent data. This procedure was repeated five times so that each subset was used once for testing.

Each classified image was subject to some postprocessing, consisting of the application of a median filter to remove isolated cells, which normally correspond to misclassifications.

The performance of each classifier with each one of the four sets of features was evaluated through the computation of the following probabilities:

1) false negatives ($p_{\mathrm{FN}} = \mathrm{FN}/(\mathrm{FN} + \mathrm{TP})$);
2) false positives ($p_{\mathrm{FP}} = \mathrm{FP}/(\mathrm{FP} + \mathrm{FN})$);
3) global errors ($p_{\mathrm{error}} = p_N \cdot p_{\mathrm{FP}} + p_P \cdot p_{\mathrm{FN}}$).

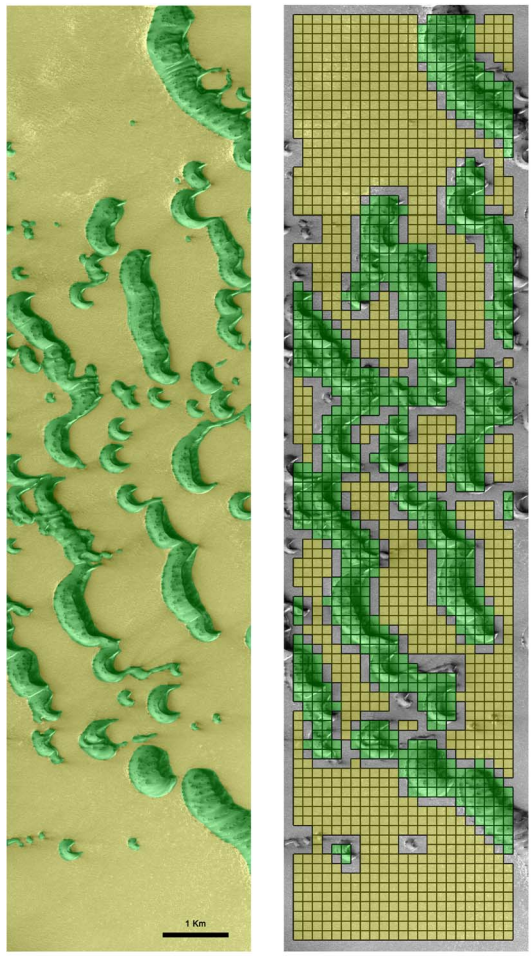

(a) (b)

Fig. 2. Ground truth overlapped to image R15-01637 ("dune" in green and "not-dune" in yellow). (a) Manual delineation and (b) tiling in cells (image credits: MSSS/NASA/JPL).

TABLE I
Fold Characteristics

Fold	*Nb. images*	*Nb. dune cells*	*Nb. non-dune cells*
1	15	8,149	12,737
2	15	8,150	9,363
3	15	8,153	13,277
4	16	8,148	16,398
5	17	8,153	18,572
Total	78	40,753	70,347

Here, FN stands for the number of false negative blocks, TN is the number of true negative blocks, FP is the number of false positive blocks, TP is the number of true positive blocks, N is the total number of negative blocks, and P is the total number of positive blocks.

The classification output is illustrated with the same MOC image for each of the two classifiers used, namely, the boosting output in Fig. 3(a) and the SVM output in Fig. 3(b).

The overall performances obtained for the complete set of images are synthesized in Table II. Globally, the values achieved are very good, with the majority of combinations presenting probabilities of error below 0.060. These refer to the feature sets HP(9), HPM(9), and HPM, with both classifiers. The exception is given by the HP features, which present inadequate results both for the boosting and SVM classifiers

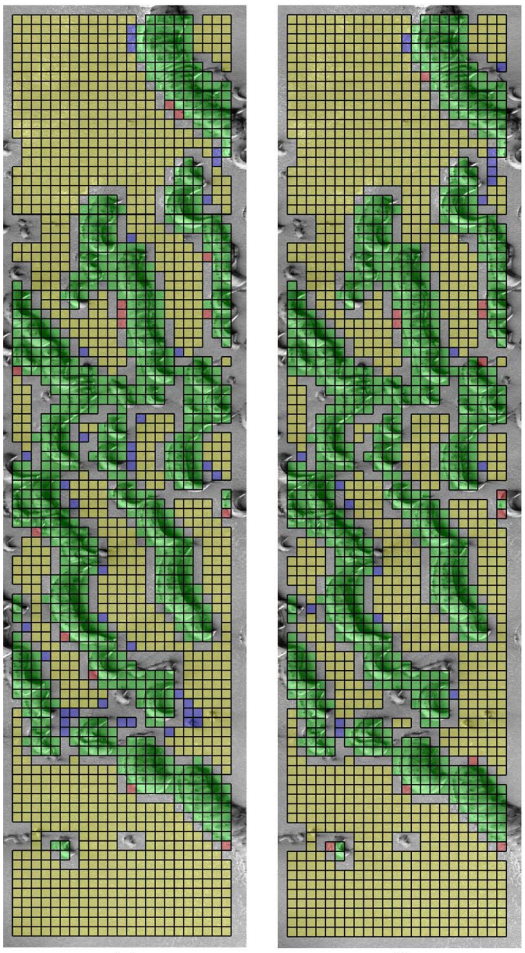

(a) (b)

Fig. 3. Classification of image R15-01637 (TP in green, TN in yellow, FN in red, and FP in blue) by (a) boosting and (b) SVM classifiers (image credits: MSSS/NASA/JPL).

TABLE II
PERFORMANCE OF BOOSTING AND SVM CLASSIFIERS

Features	Boosting			SVM		
	p_{FN}	p_{FP}	p_{error}	p_{FN}	p_{FP}	p_{error}
HP(9)	0.081	0.049	0.060	0.068	0.047	0.055
HPM(9)	0.053	0.062	0.058	0.069	0.041	**0.051**
HP	0.445	0.364	0.394	0.497	0.269	0.353
HPM	0.057	0.053	**0.054**	0.083	0.046	0.060

with a probability of error of 0.353 and 0.394, respectively. This means that the phase of the gradient is not, by itself, a discriminative feature.

Although the best performances of each classifier are achieved with different sets of features, i.e., HPM for the boosting classifier (error of 0.054) and HPM(9) for the SVM classifier (error of 0.051), the difference between them is irrelevant and similar to the values obtained with the set HP(9). There is some concordance in these results since both classifiers excel for the same three sets of features (HP(9), HPM(9), and HPM), and both have a weak performance when using the HP features. The first three sets of features use gradient and magnitude information, whereas the last set only uses phase information. This means that the gradient magnitude seems to be the most discriminative feature, and no significant advantage is observed in this problem by splitting the image block into nine cells.

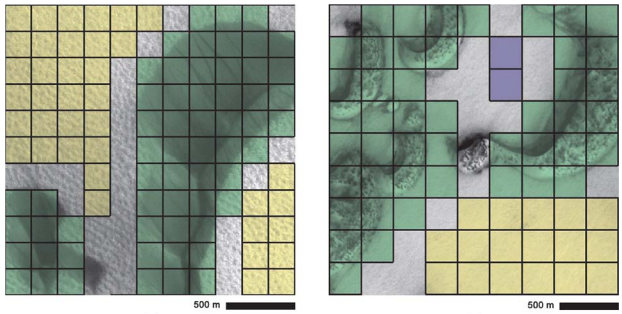

(a) (b)

Fig. 4. Details of correct detection in images differently zoomed (each cell is 40 pixels wide). (a) E03-02056. (b) R18-01147 (TP in green, TN in yellow, and FP in blue; image credits: MSSS/NASA/JPL).

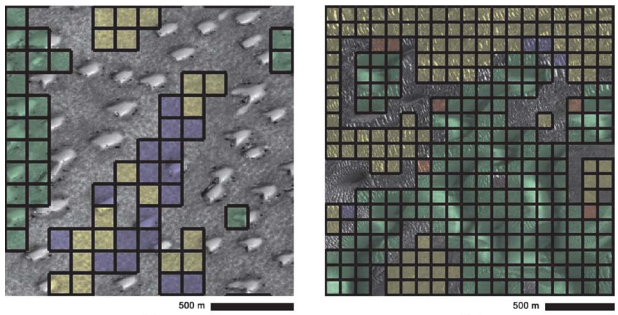

(a) (b)

Fig. 5. Details of unsolved problems in images differently zoomed (each cell is 40 pixels wide). (a) R17-02607. (b) E03-00618 (TP in green, TN in yellow, FN in red, and FP in blue; image credits: MSSS/NASA/JPL).

It is essential to carry out a detailed examination of the outputs obtained for some of the images since this permits verifying the robustness of the approaches and detecting the unsolved situations. The block size (120×120 pixels) was kept constant in all the experiments, and it has a direct influence on the performance of the classifier since the block should contain enough texture to allow the detection of dunes. If a dune occupies a small fraction of the block, it may not be detected. The contrary is also true if the dune is much larger than the block; the classifier may also fail, particularly if the block is fully contained in the dune region and there is no texture inside the dune. In such cases, the dune boundary is a key feature for the detection.

It is therefore important to check how does the method perform in the presence of very large (area $> 2 \times 2$ km) and very small (area $< 50 \times 50$ m) dunes. In Fig. 4(a), the size difference of two to three times between both dunes does not prevent their correct detection, nor that of the several structures with diversified dimensions shown in Fig. 4(b). On the contrary, dune fields constituted by similar size structures, which are much smaller than the probing cell, such as the barchan dunes shown in Fig. 5(a), are not detected in most of the situations. Another problem to solve is the presence of ripples (much smaller aeolian linear features exhibiting a parallel pattern), such as those in Fig. 5(b). Both of these situations are typical of a multiscale problem that we believe will be solved when the dimensional issue is addressed and integrated in the algorithms as part of the future developments we intend to pursue.

V. Conclusion

The high performances achieved on a large and diversified data set of images of the surface of Mars permit us to conclude that the methods tested seem to be completely adequate for the automated detection of sand dunes. Furthermore, the approach is very fast and leads to a noniterative solution, which is compatible with the large amount of data to be processed. The errors obtained indicate that the key factor resides on the selection of the features as both classifiers always achieve nearly identical performances for the same feature set, which is high for HP(9), HMP(9), and HPM and low for HP. In particular, the amplitude of the gradient has proved to be the most informative feature.

Although we have dealt only with two types of dunes (barchan and barchanoid), they represent the most common type of aeolian features on Mars, whereas the data set of images tested is representative of the diversity of sizes, shapes, and densities in distinct illumination conditions. Nevertheless, we are aware that many more different situations will have to be faced, namely, considering the scale and the diversity of the Martian landscape where many other geomorphological features can and will sometimes be present. We firmly believe that the adaptive and learning nature of the methods we are using will be able to deal with those different circumstances.

Thus, in future work, most effort will be made on the adequacy of these methods to a multiscale strategy based on multiscale features, i.e., features computed using different block sizes, so that a functional robust tool will become available to help in the cartography of Martian dunes at the planetary scale. For that purpose, we need to continue to expand the data sets by incorporating examples of other types of Martian dunes.

Additionally, the application of these methods to dunes on other planetary bodies, namely, Titan, will be tested.

We also intend to classify in an automated manner the dunes on Mars, according to the scheme used in the classification of analog terrestrial structures [20].

Acknowledgment

The authors would like to thank S. Costa for her invaluable help in the construction of the ground truth.

References

[1] R. Greeley, R. O. Kuzmin, and R. M. Haberle, "Aeolian processes and their effects on understanding the chronology of Mars," *Space Sci. Rev.*, vol. 96, no. 1–4, pp. 393–404, 2001.

[2] S. Wilson and J. Zimbelman, "Latitude-dependent nature and physical characteristics of transverse aeolian ridges on Mars," *J. Geophys. Res.—Planets*, vol. 109, no. E10, p. E10003, 2004.

[3] C. Sagan, B. A. Smith, J. Veverka, R. Tucker, E. Levintha, J. Lederber, L. Quam, P. Fox, J. B. Pollack, and R. Dubisch, "Variable features on Mars—Preliminary Mariner 9 television results," *Icarus*, vol. 17, no. 2, pp. 346–372, 1972.

[4] C. Sagan, J. Veverka, P. Fox, R. Dubisch, R. French, P. Gierasch, L. Quam, J. Lederber, E. Levintha, R. Tucker, and B. Eross, "Variable features on Mars, 2, Mariner 9 global results," *J. Geophys. Res.—Planets*, vol. 78, no. 20, pp. 4163–4196, 1973.

[5] K. S. Edgett and M. C. Malin, "New views of Mars eolian activity, materials, and surface properties: Three vignettes from the Mars Global Surveyor Mars Orbiter Camera," *J. Geophys. Res.—Planets*, vol. 105, no. E1, pp. 1623–1650, 2000.

[6] R. Hayward, K. Mullins, L. Fenton, T. Hare, T. Titus, M. Bourke, A. Colaprete, and P. Christensen, "Mars global digital dune database and initial science results," *J. Geophys. Res.—Planets*, vol. 112, no. E11, p. E1107, 2007.

[7] R. K. Hayward, K. F. Mullins, L. K. Fenton, T. N. Titus, K. L. Tanaka, M. C. Bourke, A. Colaprete, T. M. Hare, and P. R. Christensen, "Mars Global Digital Dune Database (MGD3): User's guide," in *Proc. Dunes—Planet. Dunes Workshop: Rec. Climate Change*, Alamogordo, NM, 2008, pp. 42–43, Abs. 7013.

[8] R. K. Hayward, L. K. Fenton, K. L. Tanaka, T. N. Titus, and P. R. Christensen, "Mars global digital dune database: Dune volume estimates in the north polar region," in *Proc. Lunar Planetary Sci. XLI*, Houston, TX, 2010, p. 1109, Abs. 1109.

[9] M. C. Bourke, N. Lancaster, L. K. Fenton, E. J. R. Parteli, J. R. Zimbelman, and J. Radebaugh, "Extraterrestrial dunes: An introduction to the special issue on planetary dune systems," *Geomorphology*, vol. 121, no. 1/2, pp. 1–14, 2010.

[10] L. Bandeira, J. Saraiva, and P. Pina, "Impact crater recognition on Mars based on a probability volume created by template matching," *IEEE Trans. Geosci. Remote Sens.*, vol. 45, no. 12, pp. 4008–4015, Dec. 2007.

[11] R. Martins, P. Pina, J. S. Marques, and M. Silveira, "Crater detection by a boosting approach," *IEEE Geosci. Remote Sens. Lett.*, vol. 6, no. 1, pp. 127–131, Jan. 2009.

[12] E. R. Urbach and T. F. Stepinski, "Automatic detection of sub-km craters in high resolution planetary images," *Planet. Space Sci.*, vol. 57, no. 7, pp. 880–887, 2009.

[13] H. Elbelrhiti, B. Andreotti, and P. Claudin, "Barchan dune corridors: Field characterization and investigation of control parameters," *J. Geophys. Res.—Earth Surface*, vol. 113, p. F02S15, 2008.

[14] M. Necsoiu, S. Leprince, D. M. Hooper, C. L. Dinwiddie, R. N. McGinnis, and G. R. Walter, "Monitoring migration rates of an active subarctic dune field using optical imagery," *Remote Sens. Environ.*, vol. 113, no. 11, pp. 2441–2447, Nov. 2009.

[15] P. Vermeesch and N. Drake, "Remotely sensed dune celerity and sand flux measurements of the world's fastest barchans (Bodélé, Chad)," *Geophys. Res. Lett.*, vol. 35, p. L24404, 2008.

[16] M. C. Bourke, M. Balme, R. Beyer, K. Williams, and J. Zimbelman, "A comparison of methods used to estimate the height of sand dunes on Mars," *Geomorphology*, vol. 81, no. 3/4, pp. 440–452, 2006.

[17] H. Mitasova, L. Mitas, and R. S. Harmon, "Simultaneous spline approximation and topographic analysis for lidar elevation data in open-source GIS," *IEEE Geosci. Remote Sens. Lett.*, vol. 2, no. 4, pp. 375–379, Oct. 2005.

[18] L. V. Potts, O. Akyilmaz, A. Braun, and C. K. Shum, "Multi-resolution dune morphology using Shuttle Radar Topography Mission (SRTM) and dune mobility from fuzzy inference systems using SRTM and altimetric data," *Int. J. Remote Sens.*, vol. 29, no. 10, pp. 2879–2901, May 2008.

[19] L. Bandeira, J. S. Marques, J. Saraiva, and P. Pina, "Automated detection of sand dunes on Mars," *Lecture Notes in Computer Science*, vol. 6112, pp. 306–315, 2010.

[20] E. D. McKee, "Introduction to a study of global sand seas," in *A Study of Global Sand Seas*, E. D. McKee, Ed. Honolulu, HI: Univ. Press Pacific, 1979, pp. 1–19.

[21] N. Dalal and B. Triggs, "Histograms of oriented gradients for human detection," in *Proc. CVPR Conf.*, 2005, vol. 1, pp. 886–893, New York: IEEE Press.

[22] R. E. Schapire, Y. Freund, P. Bartlett, and W. S. Lee, "Boosting the margin: A new explanation for the effectiveness of voting methods," *Ann. Stat.*, vol. 26, no. 5, pp. 1651–1686, 1998.

[23] P. Viola and M. Jones, "Robust real-time face detection," *Int. J. Comput. Vis.*, vol. 57, no. 2, pp. 137–154, May 2004.

[24] V. N. Vapnik, *The Nature of Statistical Learning Theory*. Berlin, Germany: Springer-Verlag, 1995.

[25] T. Joachims, "Estimating the generalization performance of an SVM efficiently," in *Proc. 17th Int. Conf. Mach. Learn.*, 2000, pp. 431–438, San Francisco, CA: Morgan Kaufmann.